The Astrophysical Journal, 973:145 (10pp), 2024 October 1 https://doi.org/10.3847/1538-4357/ad684c

Multiband Analysis of Strong Gravitationally Lensed Post-blue Nugget Candidates from the Kilo-degree Survey

Rui Li[1,2], Nicola R. Napolitano[3,4,5], Linghua, Xie[4], Ran Li[2,6], Xiaotong Guo[7], Alexey Sergeyev[8,9], Crescenzo Tortora[10], Chiara Spiniello[10,11], Alessandro Sonnenfeld[12], Léon V. E. Koopmans[13], and Diana Scognamiglio[14]
[1] Institude for Astrophysics, School of Physics, Zhengzhou University, Zhengzhou 450001, People's Republic of China; liruiww@gmail.com
[2] National Astronomical Observatories, Chinese Academy of Sciences, 20A Datun Road, Chaoyang District, Beijing 100012, People's Republic of China
[3] Department of Physics "E. Pancini," University Federico II, Via Cinthia 6, 80126-I, Naples, Italy; nicolarosario.napolitano@unina.it
[4] School of Physics and Astronomy, Sun Yat-sen University, Zhuhai Campus, 2 Daxue Road, Xiangzhou District, Zhuhai, People's Republic of China
[5] CSST Science Center for Guangdong-Hong Kong-Macau Great Bay Area, Zhuhai 519082, People's Republic of China
[6] School of Astronomy and Space Science, University of Chinese Academy of Sciences, Beijing 100049, People's Republic of China
[7] Institute of Astronomy and Astrophysics, Anqing Normal University, Anqing, Anhui 246133, People's Republic of China
[8] Université Côte d'Azur, Observatoire de la Côte d'Azur, CNRS, Laboratoire Lagrange, France
[9] V. N. Karazin Kharkiv National University, Kharkiv, 61022, Ukraine
[10] INAF—Osservatorio Astronomico di Capodimonte, Salita Moiariello 16, 80131—Napoli, Italy
[11] Department of Physics, University of Oxford, Denys Wilkinson Building, Keble Road, Oxford OX1 3RH, UK
[12] Department of Astronomy, School of Physics and Astronomy, Shanghai Jiao Tong University, Shanghai 200240, People's Republic of China
[13] Kapteyn Astronomical Institute, University of Groningen, P.O.Box 800, 9700AV Groningen, The Netherlands
[14] Jet Propulsion Laboratory, California Institute of Technology, 4800, Oak Grove Drive, Pasadena, CA 91109, USA
Received 2023 October 16; revised 2024 July 25; accepted 2024 July 26; published 2024 September 27

Abstract

During the early stages of galaxy evolution, a significant fraction of galaxies undergo a transitional phase between the "blue nugget" systems, which arise from the compaction of large, active star-forming disks, and the "red nuggets," which are red and passive compact galaxies. These objects are typically only observable with space telescopes, and detailed studies of their size, mass, and stellar population parameters have been conducted on relatively small samples. Strong gravitational lensing can offer a new opportunity to study them in detail, even with ground-based observations. In this study, we present the first six bona fide samples of strongly lensed post-blue nugget (pBN) galaxies, which were discovered in the Kilo Degree Survey. By using the lensing-magnified luminosity from optical and near-infrared bands, we have derived robust structural and stellar population properties of the multiple images of the background sources. The pBN galaxies have very small sizes of $R_{\rm eff} < 1.3$ kpc, high mass density inside 1 kpc of $\log(\Sigma_1/M_\odot\ {\rm kpc}^{-2}) > 9.3$, and low specific star formation rates of $\log({\rm sSFR\ Gyr}^{-1}) \lesssim 0$, The size–mass and Σ_1–mass relations of this sample are consistent with those of the red nuggets, while their sSFR is close to the lower end of compact star-forming blue nugget systems at the same redshift, suggesting a clear evolutionary link between them.

Unified Astronomy Thesaurus concepts: Strong gravitational lensing (1643); Galaxy evolution (594); Einstein rings (451)

1. Introduction

According to the hierarchical galaxy formation scenario (e.g., Renzini 2006; Lapi et al. 2018), large primordial disk galaxies undergo a dissipative process in which gas streams from the cosmic web fall into the disks, concentrate in the central region, and lead to a high rate of star formation (Dekel et al. 2009). This process results in the formation of extremely compact and star-forming galaxies (SFGs), known as "blue nuggets" (Barro et al. 2013, 2014; Zolotov et al. 2015, hereafter Z+15; Tacchella et al. 2016). They are characterized by a very small effective radius, $R_{\rm eff} < 1$ kpc (e.g., Williams et al. 2014, hereafter W+14; Z+15), high surface density inside the central 1 kpc, $\log(\Sigma_1/M_\odot\ {\rm kpc}^{-2}) > 9.0$ (e.g., Barro et al. 2013; Dekel & Burkert 2014), and a high specific star-forming rate, $\log({\rm sSFR\ Gyr}^{-1}) > 0$ (e.g., Z+15; Huertas-Company et al. 2018, hereafter HC+18). The lifetime of these blue nuggets can be quite short (<1 Gyr), as they are expected to quickly switch off their star formation and turn into post-blue nuggets (pBNs) of similar structural properties (Dekel & Burkert 2014; Z+15) but lower sSFR of $\log({\rm sSFR/Gyr}) \lesssim 0$. The actual mechanisms behind these "quick" transformations are yet to be clarified. They are thought to consist of the combined effect of feedback from star winds induced by strong starbursts and the presence of active galactic nuclei (AGN; e.g., Dekel & Silk 1986; Murray et al. 2005; Z+15; Cattaneo et al. 2009). These mechanisms should be effective over a short timescale (∼1 Gyr or less) and at higher redshifts ($z > 2$, Dekel & Burkert 2014; Costantin et al. 2021). After complete quenching, the pBNs turn into compact red nuggets, which finally grow in mass and size through dry merging, forming present-day elliptical galaxies (e.g., Newman et al. 2012; Oser et al. 2012; Nipoti et al. 2012; Posti et al. 2014; Spiniello et al. 2021).

If the red nuggets indeed evolved from blue nuggets, there must be a continuum between some basic properties (e.g., stellar mass–M_*, age, specific star-forming rate (sSFRs), effective radius ($R_{\rm eff}$), and surface density inside 1 kpc–Σ_1, see, e.g., Tacchella et al. 2016) of blue nuggets, pBNs, and red nuggets (see, e.g., HC+18). Hence, studying the relationships between these properties (e.g., $R_{\rm eff}-M_*$, sSFR$-M_*$, and

$\Sigma_1 - M_*$) can help us better understand their evolutionary path and determine their roles in the galaxy evolution scenario. This evolutionary track has been investigated in simulations by Z+15, showing that the majority of compaction of blue nuggets begins when $\log(M_*/M_\odot) < 9.5$ and $R_{\rm eff} > 1$ kpc, followed by quenching $\log(M_*/M_\odot) \sim 10$ and $R_{\rm eff} < 1$ kpc. This compaction phase occurs up to $z \sim 2$. Furthermore, galaxies with larger masses experience quenching at a higher value of Σ_1, whereas lower-mass galaxies quench at lower values of Σ_1. As blue nuggets transit into red nuggets, their size begins to increase linearly with mass along the passive galaxy size–mass relation. On the observational side, the size–mass relation of red nuggets has been investigated through direct observations (e.g., Damjanov et al. 2009, hereafter D+09) or the strong lensing (SL) magnification effect (Oldham et al. 2017). Although a few blue nuggets have also been found and confirmed (Marques-Chaves et al. 2022), their size–mass relation remains poorly constrained (see, e.g., W+14), mainly because the sizes of this kind of galaxies are difficult to measure.

SL can provide powerful observational support to systematically study these objects. The warped geometry of the space and time generated by the gravitational field of massive objects (lenses) in the Universe produces a magnification of the luminosity of the background "lensed" galaxies. This is particularly efficient for compact sources, which can be studied in much greater detail (Oldham et al. 2017), even with ground-based observations (Napolitano et al. 2020). For example, Toft et al. (2017) analyzed a strongly lensed red nugget and suggested that the stars in this galaxy formed in a disk rather than a merger-driven nuclear starburst. Two Einstein crosses from pBNs have been discovered and confirmed with Very Large Telescope (VLT)/MUSE observations by (Napolitano et al. 2020, hereafter N+20) in the footprint of the Kilo Degree Survey (KiDS; de Jong et al. 2013). This finding has shown the path for systematic studies of pBNs via quadruple lensing events in future ground and space large sky surveys, where thousands of similar systems have been predicted to be found (see the discussion in N+20). In N+20, we estimated the expected number of the lensed pBNs in KiDS (namely, half a dozen for sources at $z < 4$), where we did not concentrate on all potential candidates in the surveyed area but only on the two pBNs that had been spectroscopically confirmed. In this work, we instead add all previously unexplored candidates despite the absence of spectroscopic data for them. The purpose of this paper is to fully introduce a comprehensive optical and near-infrared (NIR) ray-tracing analysis that, without spectroscopy, can allow us to derive the photometric redshifts (photo-zs) for both the foreground lensing galaxy and the background source, thus photometrically confirming the lensing nature of the systems. Here, we also discuss that, in addition to confirmation, the method can allow us to characterize the properties of the background sources and derive their scaling relations so that we can use them to compare with those of the red nuggets and discuss an evolutionary link with them.

The paper is organized as follows. Section 2 describes the data used in this study. Section 3 outlines the main methods used for lens modeling, photo-z estimation, and determination of stellar population parameters. Section 4 discusses the multiband ray-tracing results and the scaling relations of the six lensed pBNs. Finally, Section 5 concludes our study. For all calculations, we assume a ΛCDM cosmology with (Ω_M, Ω_Λ, h) = (0.3, 0.7, 0.7).

2. Data

The data used in this analysis consist of optical images from the KiDS and NIR images from the VISTA Kilo-degree Infrared Galaxy (VIKING) surveys. KiDS covers a total area of 1350 deg^2 in four optical filters (u, g, r, i). The seeing, measured by the full width at half-maximum (FWHM), ranges from approximately 0.″7 to 1.″1 across all the bands, with the r-band image being the sharpest one (median FWHM $\sim$ 0.″7). The mean limiting AB magnitude (5σ level within a 2″ aperture) are 24.23 ± 0.12, 25.02 ± 0.13, 25.12 ± 0.14, and 23.68 ± 0.27, in the u, g, r, i bands, respectively (see Kuijken et al. 2019 for more details). The VIKING survey (see Edge et al. 2013) covers the same area as KiDS but through five different NIR bands (Z, Y, J, H, K_s). The median seeing for these images is around 0.″9 and the AB magnitude depths are 23.1, 22.3, 22.1, 21.5, and 21.2, in all filters, respectively (see Sutherland et al. 2015 for more details).

In the KiDS survey, we have identified 268 high-quality SL candidates using mainly a Deep Learning approach (Petrillo et al. 2019; Li et al. 2020, 2021). To assemble a collection of lensed pBNs, we conducted a visual examination of the *gri* composited stamps of these candidates. This process resulted in 14 SL candidates that potentially exhibit pBN sources. Each of them shows blue lensed images, with at least one image appearing pointlike, indicating that the background sources are compact, similar to the lensed pBNs in N+20. Among these 14 candidates, two systems have more than one foreground lens, which would make the lens modeling very uncertain. For six of the remaining 12 candidates, we encountered substantial difficulties in discerning the lensed images across at least three NIR bands, even after subtracting the foreground light before performing the strong lens modeling. This is due partially to the shallower depth of the VIKING data, but also to the properties of the spectral energy distribution (SED) distribution of high-z background sources, very likely young systems. Indeed, for younger systems at high z we might expect a faint NIR (see also W+14, their Figure 17). In this respect, the visibility in NIR tend to naturally select the older systems, that are more compatible with a pBN phase. In fact, the limiting magnitudes of different bands in the VIKING survey are $\mathrm{mag_{AB}} \lesssim 23$ and SFGs with rest-frame optical band magnitudes around 23–24 AB will be hard to detect, even if they are magnified by lensing. This is an important selection effect to keep in mind in the following analysis. Finally, we are left with six SL systems with optical+NIR imaging data good enough for the analysis we aim to perform in this work. In Figure 1, we show the *gri* color combined images of the final six SL candidates (KiDSJ023929−321129, KiDSJ122456+005048, KiDSJ224546−295559, KiDSJ230226−335637, KiDSJ232940−340922, and KiDSJ234804-302855) used for this analysis. KiDSJ122456+005048 and KiDSJ232940-340922 are the two lensed pBNs observed with MUSE spectroscopy from N+20. We keep these "confirmed" cases in the sample to check if, with the pure photometric approach proposed here, we obtain consistent results in terms of the redshifts of the lenses and the sources. We also note that KiDSJ023929+321129 was studied by Sergeyev et al. (2018) as a gravitational quadruple lens candidate without giving the redshift of the sources.

The magnification effect of this SL sample, combined with the nine-band optical images from the KiDS and VIKING survey, enables the accurate reconstruction of the light distribution of the background sources and the subsequent determination of their photo-zs. These data are the foundation

Table 1
Source Properties from the Multiband Ray-tracing Flexible Model

ID	$R_{\rm eff}$ (arcsec)	b/a	p.a. (deg)	n_r	u (mag)	g (mag)	r (mag)	i (mag)	Z (mag)	Y (mag)	J (mag)	H (mag)	Ks (mag)
J023929−321129	0.063 ± 0.002	0.40 ± 0.02	89	2.7 ± 0.1	23.70	23.29	23.14	23.21	23.08	23.44	22.48	22.49	22.11
J122456+005048[a]	0.057 ± 0.002	0.53 ± 0.04	163	0.8 ± 0.1	⋯	24.05	23.67	23.14	22.52	22.24	21.91	21.88	21.67
J224546−295559	0.054 ± 0.006	0.46 ± 0.05	16	3.4 ± 0.5	24.02	23.90	23.73	23.72	23.20	22.79	22.62	⋯	⋯
J230226−335637	0.154 ± 0.008	0.52 ± 0.05	61	1.8 ± 0.3	23.38	22.89	22.96	22.74	22.94	22.62	22.14	21.89	22.56
J232940−340922[a]	0.071 ± 0.011	0.26 ± 0.08	161	1.1 ± 0.2	⋯	23.68	23.52	23.53	23.39	22.86	22.52	22.12	21.86
J234804−302855	0.144 ± 0.007	0.38 ± 0.03	71	1.5 ± 0.2	23.93	23.70	23.88	23.78	24.38	23.55	23.22	22.83	⋯

Notes. Column (1) is the KiDS ID, in the form of hh-mm-ss and deg-mm-ss. Columns (2)–(5) list the source parameters from the lensing model by assuming a Sérsic profile for the sources. From left to right are the effective radius $R_{\rm eff}$ in the unit of arcsec, the minor-to-major axis ratio b/a, the position angle p.a., and the r-band Sérsic index n_r, respectively. The Sérsic indexes are fixed to the r-band value when modeling other band images. Columns (6)–(14) list the magnitudes of each source obtained from the flexible lensing model (see the text for details). Errors in magnitudes are shown in Figure 3.
[a] These are the two pBNs that have been studied in N+20 with MUSE spectroscopy and reanalyzed here to check the consistency of the nine-band lensing approach.

of a detailed stellar population analysis via the SED fitting, which will finally provide us an estimate of the specific star formation rate (sSFR) of the background galaxies and assess the pBN nature of the sources.

3. Methods and Model Parameters

In this section we describe the methods adopted to (1) perform the ray-tracing models of the SL systems in optical and NIR images; (2) derive the structural parameters of the background sources; (3) use the "unlensed" multiband photometry and colors to estimate the photo-zs and the stellar population parameters of the sources; (4) use the source decontaminated fluxes of the foreground lenses to obtain their photo-zs. Following N+20, we expect these systems to show high-z ($z > 1$), blue, ultracompact background sources with sSFR compatible with quenched systems.

3.1. Lens Modeling

For the ray-tracing modeling of the optical and NIR bands, we use `Lensed` (Tessore et al. 2016), which implements a Markov Chain Monte Carlo method to look for the best-fitting parameters of the mass of the lens and the light of both the lens and background source. The lensing model is convolved with a point-spread function obtained by fitting one nearby star to the lens system with two Moffat profiles. For the light distribution of the source, we assume a Sérsic profile (Sersic 1968), where the free parameters are n, the Sérsic index, $R_{\rm eff}$, the effective radius, x_0 and y_0, the center coordinates, q, the axis ratio, and p.a., the position angle. The light of the lens is assumed to follow an elliptical de Vaucouleur profile (de Vaucouleurs 1948), which corresponds to a special case of Sérsic profile with $n = 4$. The total mass of the lens is modeled with a singular isothermal ellipsoid profile (Kormann et al. 1994), and its projected two-dimensional surface mass density profile is described by

$$\Sigma(x, y) = \frac{1}{2}\Sigma_{\rm c}\ \sqrt{q}\ \theta_{\rm E}\ (x^2 + q^2y^2)^{-1/2}, \quad (1)$$

where θ_E is the lensing strength, equivalent to the Einstein radius, and q is the minor-to-major axis ratio of the isodensity contours. $\Sigma_{\rm c} = c^2/(4\pi G)(D_{\rm s}/D_{\rm d}D_{\rm ds})$ is the critical density, where $D_{\rm s}$ and $D_{\rm d}$ are the angular diameter distances from the observer to the lens and the source, respectively, and $D_{\rm ds}$ is the distance between the lens and source. We also include the external shear, $\gamma_{\rm ext}$, which approximates the influence of the surrounding environment on the lensing potential. Finally, we have 16 parameters for the source, mass, and foreground light, all together.

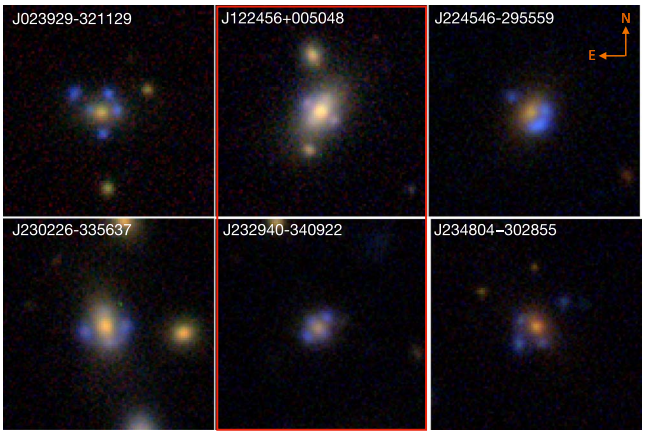

Figure 1. Colored stamps ($20'' \times 20''$) of the six lensed blue nuggets, obtained by combining g-, r-, and i-band images from KiDS. Each system exhibits three or four pointlike images, indicating that the background sources may be very small in size. The two systems highlighted in red have been confirmed with MUSE/VLT spectroscopy in N+20.

As reference band for the ray-tracing model, we use the r-band images, as they provide the best image quality with an average seeing of FWHM $= 0.''68$. As shown in N+20, this, combined with the pixel scale of $0.''2\,{\rm px}^{-1}$ of the camera (Kuijken et al. 2019), is suitable to derive the structure parameters of the background sources, whose images are of the order of a few pixels (see Figure 1). The best-fitting r-band parameters of the sources, obtained with "Lensed," are reported in Table 1. The $\chi^2/{\rm dof}$ obtained from the lensing modeling is always between 0.8 and 1.2, meaning that the six SL systems are accurately modeled. The intrinsic r-band AB magnitudes of the sources are between 23 and 24.7 and the effective radii, $R_{\rm eff}$, are between $0.''05$ and $0.''15$. These galaxies, faint in brightness and very compact in size, are hard to be directly resolved, even by space telescopes like HST. The Sérsic index of the sources is between $0.8 < n < 3.5$, indicating that some of them are likely to be disk galaxies ($n < 2$), while some others have an n index closer to spheroids ($n > 2$). We remark that, for the two previously studied systems in N+20, where a different ray-tracing tool was adopted, we have found larger n values (but yet all consistent with disk systems, i.e., $n \lesssim 1$), while the $R_{\rm eff}$ is consistent within 20%. This shows that the size is a

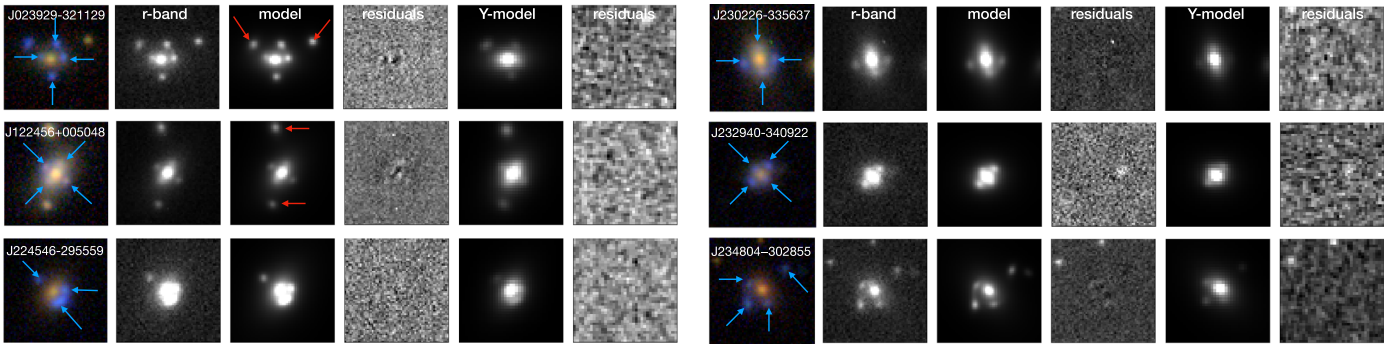

Figure 2. Ray-tracing model of the selected systems shown in Figure 1. From left to right: (1) the color image; (2) the *r*-band image; (3) the lensed *r*-band image model; (4) the *r*-band model-subtracted image; (5) the *Y*-band image model; (6) the *Y*-band model-subtracted image. The blue arrows point to the lensed images, while the red arrows show other projected galaxies in the field of view.

rather robust parameter, while the Sérsic index is more uncertain.

For all other three optical bands (*ugi*) from KiDS and five NIR bands (*ZYJHKs*) from VIKING, we use the same lens modeling set-up as for the *r* band. However, the image quality of these eight bands is usually worse than the quality of the *r*-bands images, mainly because of the poorer seeing (which is set to $<0\farcs7$ only for the *r* band, according to the KiDS and VIKING survey strategies), but also for the lower SNR, especially in NIR (see Section 2). This requires some strategies to optimize the fidelity of the multiband models.

We start with modeling the six systems by maximizing the number of free parameters in all bands.[15] In this "flexible" prior approach, we fix the values of a few model parameters to those obtained in the *r*-band images. First, the position angle p.a., and the axis ratio q for the lens mass and the external shear. This is reasonable, as the mass model is independent of the band and the *r* band is expected to give the best constraints. We also check that the Einstein radius computed from each of the other bands is consistent within the errors with the one found on the *r* band. This leaves some freedom for the mass model to incorporate the effect of data noise in the different bands. Second, we also fix the axis ratio q and Sérsic index for the background sources. This is also reasonable, as the KiDS and VIKING bands will correspond to NUV and optical rest-frame bands if these are placed at $z > 1$, and there is little evidence of strong color gradients at these wavelengths in either compact star forming (e.g., Liu et al. 2016) or quiescent galaxies (e.g., Whitaker et al. 2012).

The final modeled magnitudes of the source of each lens, using this approach, are listed in Table 1, while in Figure 2, we show the ray-tracing models of the *r* band, as representative of optical bands, and the *Y* band, as representative of NIR bands. As a sanity check, we have also performed another round of models, where this time we have minimized the free parameters among the nine bands. In particular, for the *r* band we used the same approach as above, while for other bands, we used the *r*-band parameters to fix the effective radius $R_{\rm eff}$ of the foreground lens, the θ_E, q, and p.a. of the masses, the external shear, as well as the $R_{\rm eff}$, n, q, and p.a. of the sources. Although these "frozen" priors are based on stronger assumptions than the flexible ones, they reduce the freedom of the ray-tracing model to find arbitrary solutions that might impact the main parameters we are interested in, i.e., the source magnitudes. The results of the frozen prior models are reported in the Appendix, where we show that the source magnitudes are not significantly affected by the two extreme approaches and discuss the comparison with the flexible prior results in detail.

3.2. Photo-zs and Stellar Population Parameters of the Sources from SED Fitting

Source redshifts are essential for two main reasons: (1) to confirm the high-z nature of the multiple images and (2) to convert the angular sizes in arcsec into the physical scales in kiloparsec to be used for the scaling relations. As we have spectroscopic redshifts (spec-zs) for two systems only (i.e., the two systems previously analyzed by N+20), we use the SED fitting of the nine-band photometry of the sources to determine the photo-zs. This approach has been found to be reasonably accurate for normal lenses using optical imaging from ground-based observations (see a.g. Langeroodi et al. 2023). In our case, the unique availability of the NIR and the higher lensing model accuracy allowed by pseudo-cross lensing configurations (Gu et al. 2022), suggesting that we can reach possibly a similar or better accuracy. As a sanity check for our approach, we can also use the two N+20 lenses, for which we have the spec-zs for both the sources and deflectors, hence providing a direct validation of our photo-z estimates.

The SED fitting is performed with `Lephare` (Ilbert et al. 2006) using as input the multiband photometry of the pBNs derived with the lensing analysis as in Table 1. Here, we adopt the BC03 (Bruzual & Charlot 2003) stellar population synthesis models, a Chabrier (Chabrier 2003) stellar initial mass function (IMF) and an exponentially decaying star formation history. As we expect these systems to be compact, poorly star-forming, old systems, we assume solar metallicity (as found for previous lensed pBNs in N+20[16]), while all other parameters, such as the e-folding time, age of the main stellar population, and internal extinction, $E(B-V)$, are free to vary. For each of the six pBNs, we let the redshift vary in the range of (0, 4), and require `Lephare` to output the best-fitting parameters, e.g., photo-zs, stellar mass, age, SFRs, and their corresponding errors. The resulting photo-zs, as well as other stellar population parameters, are shown in Table 2. To check

[15] We notice that three systems have almost no signals from both the foreground and background galaxies in the *u* band and three systems have very faint lensed images in the K_s band, making the lens modeling in these bands impossible to perform.

[16] However, the assumption of solar metallicity is rather conservative for high-z galaxies. Using more realistic lower metallicities would produce higher ages (Worthey 1994; Trager & Somerville 2009), hence reinforcing the evidence of old stellar populations in the source galaxies.

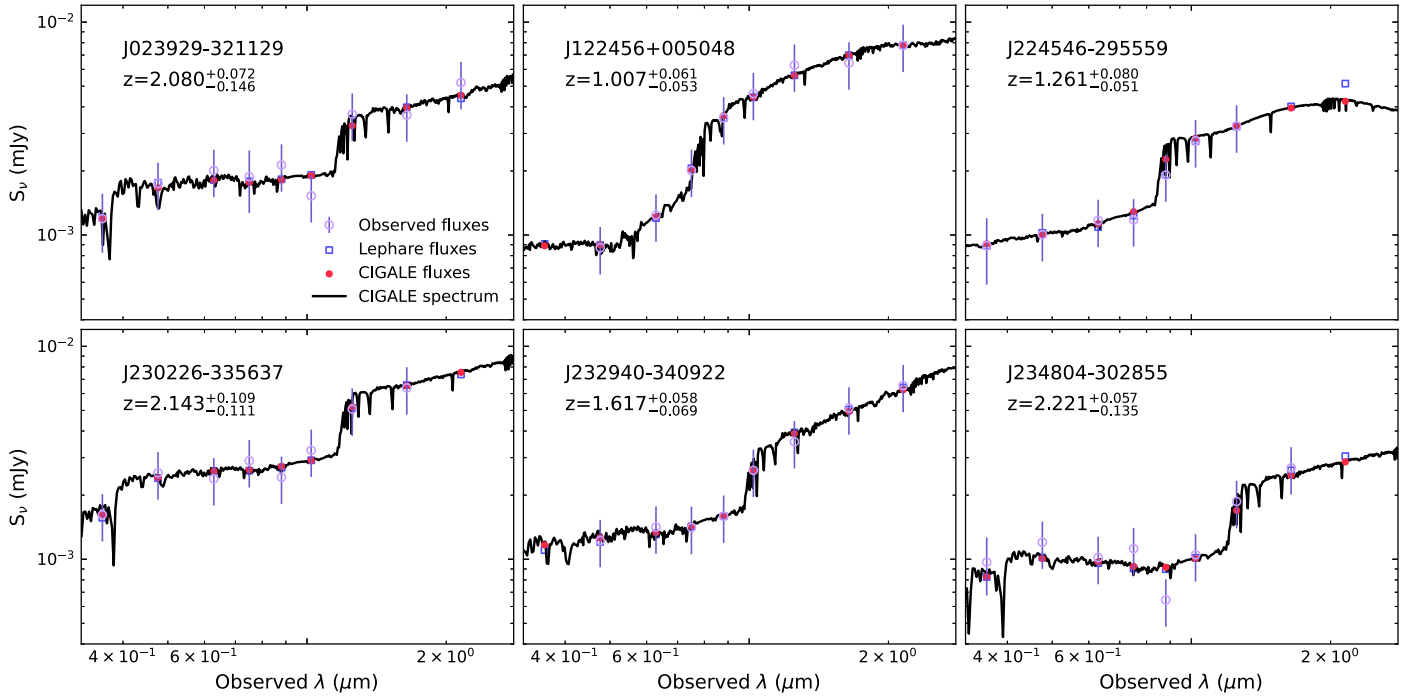

Figure 3. The SED fitting results from `Lephare` and `Cigale` for the six source galaxies. In each panel, we show the observed multiband flux from the lensing model (purple circles with error bars), the template flux from `Lephare` (blue squares), and the template spectrum from `Cigale` (black solid line) and its corresponding template flux (red dots). The 4000 Å break can be clearly seen in the spectra and the template flux, and their locations are consistent with the fitted photo-zs.

Table 2
Stellar Population Properties of the Blue Nuggets as in Table 1

$z_{\rm photo}^{\rm lens}$	$z_{\rm photo}^{\rm src}$	$R_{\rm eff}$ (kpc)	log$M_{*\rm Le}$ ($M_\odot$)	log$M_{*\rm Ci}$ ($M_\odot$)	log(sSFR)$_{\rm Le}$ (Gyr^{-1})	log(sSFR)$_{\rm Ci}$ (Gyr^{-1})	age$_{\rm Le}$ (Gyr)	age$_{\rm Ci}$ (Gyr)	$\Sigma_{1\rm Le}$ ($M_\odot$/kpc^2)	$\Sigma_{1\rm Ci}$ ($M_\odot$/kpc^2)
$0.46^{+0.07}_{-0.09}$	$2.08^{+0.07}_{-0.15}$	0.52 ± 0.02	$10.05^{+0.19}_{-0.06}$	10.32	0.43	0.09	0.5	2.0	9.40	9.66
$0.31^{+0.22}_{-0.08}$	$1.01^{+0.06}_{-0.05}$	0.46 ± 0.02	$10.16^{+0.02}_{-0.21}$	10.10	−0.94	−0.84	4.5	4.0	9.61	9.55
$0.51^{+0.04}_{-0.05}$	$1.26^{+0.08}_{-0.05}$	0.45 ± 0.05	$9.98^{+0.08}_{-0.25}$	9.94	−0.30	0.13	2.0	2.0	9.35	9.30
$0.47^{+0.04}_{-0.11}$	$2.14^{+0.11}_{-0.11}$	1.28 ± 0.07	$10.49^{+0.09}_{-0.23}$	10.41	0.01	0.40	1.0	1.0	9.62	9.54
$0.63^{+0.09}_{-0.07}$	$1.62^{+0.06}_{-0.07}$	0.61 ± 0.09	$10.44^{+0.01}_{-0.25}$	10.44	−0.36	−0.30	3.0	4.0	9.76	9.76
$0.49^{+0.20}_{-0.04}$	$2.22^{+0.06}_{-0.14}$	1.19 ± 0.06	$10.23^{+0.01}_{-0.21}$	10.18	−0.36	−0.20	2.5	3.0	9.36	9.31

Note. Column (1) shows the best-estimated lens photo-zs ($z_{\rm photo}^{\rm lens}$) from `Lephare`. Column (2) shows the corresponding source photo-zs ($z_{\rm photo}^{\rm src}$). Column (3) shows the effective radius $R_{\rm eff}$ in units of kiloparsec. Columns (4)–(11) list the main stellar population parameters from both `Lephare` and `Cigale` (Le and Ci subfixes, respectively). From left to right are the stellar mass log($M_*/M_\odot$), specific star formation rate log(sSFR), the age, and the surface mass densities within the central 1 kpc Σ_1, respectively.

the robustness of our photo-z estimates, we verify the consistency of the results from the flexible and frozen models (see Section 3.1). The comparison between the two models (see also Appendix) shows that the photo-zs from different models are consistent within the typical errors expected for high-z galaxy photo-zs from ground-based observations (e.g., van den Busch et al. 2020; Amaro et al. 2021; Li et al. 2022). The flexible result also shows that the N+20 objects have photo-zs of $1.01^{+0.06}_{-0.05}$ and $1.62^{+0.06}_{-0.07}$, respectively, which are fully consistent with their spec-zs (i.e., 1.101 and 1.589, respectively).

The source redshifts of the six SL systems cover the range of $1.0 \lesssim z \lesssim 2.3$. In Figure 3, we show the observed fluxes and the best-fitted SED templates for the sources for the flexible model only. The best fit of the multiband photometry is remarkably good in all cases. In particular, the NIR bands are essential to closely map the rest-frame 4000 Å break, which is essential in the photo-z determination.

As a consistency check, to make sure that the parameters obtained by `Lephare` are tool-independent, we repeat the same analysis with `Cigale` v2018.0 (Boquien et al. 2019). Since this latter is not designed to predict photo-zs, we fix the redshift of each source to the photo-zs from `Lephare`. The resulting stellar mass and age of the sources (see Table 2) are consistent with `Lephare` estimates. We observed that the sSFRs derived from the `Cigale` show values that are close to the ones of `Lephare`, except for J023929−321129, and assuming typical errors on sSFR from `Lephare` (∼0.4 dex; see Xie et al. 2023) they are all consistent within 1σ. As `Cigale` does not provide uncertainties on the best-estimated parameters, we will use `Lephare` results as a reference for stellar population parameters in the following. We finally remark that all stellar population estimates are also consistent with the ones obtained with the frozen model magnitudes, within the typical statistical errors of stellar populations, as discussed in the Appendix.

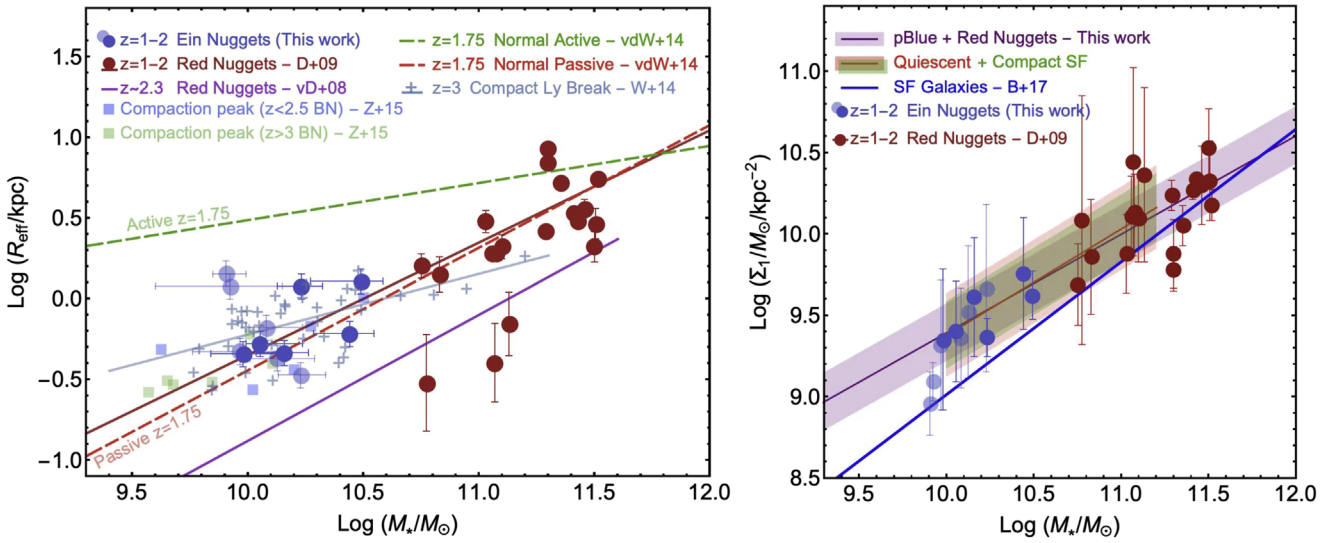

Figure 4. Left: size–mass relation of the pBNs (blue dots) and other galaxies from literature, i.e., (1) red nuggets at $1 < z < 2$ and their linear fit (red dots and red solid line, Damjanov et al. 2009, D+09), and linear fit to the red nuggets at $z \sim 2.3$ (purple line, van Dokkum et al. 2008, vD+08); (2) the compaction peak of blue nuggets at $z < 2.5$ (green squares) and $z > 3$ (blue squares) in simulations (Zolotov et al. 2015, Z+15); (3) the compact LBGs at $z \sim 3$ and their linear fit (blue crosses and blue solid line); (4) linear fit to the measurements of normal passive (red dash lines) and active (green dash lines) galaxies at $z = 1.75$ (van der Wel et al. 2014, vdW+14). All of the stellar masses of the pBNs have been corrected to Chabrier IMF. Right: Σ_1–M_* relation of the pBNs (blue dots) and red nuggets (red dots) at $1 < z < 2$ from D+09. The solid purple line is the best-fit relation, while the purple shaded area represents the 1σ error of the fitted relation. We also plot the same relationship for samples of quiescent galaxies (red shaded area), compact SFGs (green shaded area), and the normal SFGs (blue line) from (Barro et al. 2017, B+17). In both plots, it is clear that the pBNs follow the trend of the passive galaxies and red nuggets, rather than standard active galaxies at the same redshift.

Finally, in Table 2, we also report the photo-zs of the foreground lenses, that have been derived following the same procedure for the source photo-zs. The details of this part of the analysis are beyond the purpose of this paper and will be the focus of an upcoming ray-tracing analysis. Here we just remark that all the systems are consistent with being lensing events, as the redshifts of the central galaxies are lower than the one of the background sources. The photo-zs of the lenses of the two spectroscopic systems from N+20 are $0.31^{+0.22}_{-0.08}$ and $0.63^{+0.09}_{-0.07}$, respectively; both are higher than their spec-zs of 0.237 and 0.381. The former aligns well with the spec-zs, within approximately one standard deviation (1σ) of error. However, the latter exhibits a discrepancy greater than 3σ. We intend to reserve further refinement of these foreground redshifts in future research.

4. Results and Discussion

In this section, we concentrate on the results obtained with the flexible model, while the ones from the frozen approach are discussed in the Appendix. We start by using the photo-zs derived in Table 2 to convert the effective radii $R_{\rm eff}$ into the physical scale. We find that all sources have $R_{\rm eff}$ smaller than 1.5 kpc, while stellar masses are in the range of $9.9 < \log(M_*/M_\odot) < 10.5$, as reported in Table 2. In the same table, the surface mass densities within 1 kpc are listed and are larger than $\log(\Sigma_1/M_\odot {\rm kpc}^2) \sim 9.3$. These numbers make the sources consistent with typical parameters of blue nuggets (e.g., Z+15; Tacchella et al. 2016; Barro et al. 2017, hereafter B+17). The ages of these galaxies are generally older than 1.0 Gyr, except for J023929-321129, which has an age of only 0.5 Gyr. The two N+20 systems remain the oldest ones in the sample with the new SL-based nine-band photometry, showing ages of 4.5 (J122456+005048) and 3 (J232940 −340922) Gyr. This exhibits a less than 35% discrepancy when compared to the ages previously reported in the N+20 study, which were 3.8 Gyr and 4.5 Gyr, respectively. All systems show low sSFRs, i.e., $\log({\rm sSFR\ Gyr}^{-1}) \lesssim 0.4$, which is consistent with the definition of quiescent systems (see Johnston et al. 2015; Z+15; B+17; HC+18). In conclusion, in line with the findings presented in N+20, these systems are all fully compatible with being pBNs.

Further support for this conclusion comes from other similar results obtained in literature: (1) in terms of the SFR–M_*[17] relation (Johnston et al. 2015, see their Figure 6) show that for galaxies with masses of $9.9 \lesssim \log(M/M_\odot) \lesssim 10.5$, the transition place between SFGs and passive galaxies occurs at $0.5 \lesssim \log({\rm SFR}/M_\odot\ {\rm yr}^{-1}) \lesssim 1.5$, compatible to what found for our pBN sample, $0.2 \lesssim \log({\rm SFR}/M_\odot\ {\rm yr}^{-1}) \lesssim 1.5$ (calculated from Table 2[18]); (2) in terms of the sSFR–Σ_1 relation, HC18 show that the pBNs at $1.4 < z < 2.2$, and with a central mass density of $\log(\Sigma_1/M_\odot {\rm kpc}^{-2}) \gtrsim 9.0$, have $-1.5 \lesssim \log({\rm sSFR\ Gyr}^{-1}) \lesssim 0$. This latter study also shows that the density of pBNs in the above mass and redshift ranges is higher than the density of blue nuggets. For this reason, and for the "selection effect" from the faint NIR photometry, making us a little sensitive to strong star-forming systems at $z > 1$, as discussed in Section 2, we tend to select blue (due to the depth in optical bands), compact (due to the strong lensing effect) systems with low star formation rate, all conspiring toward a selection of pBNs.

The size–mass relation for the six pBNs is plotted in the left panel of Figure 4 (blue solid circles). Here, we also show (1) red nuggets at $z \sim 1.5$ from D+09 (red solid circles, and best-fit linear line) and at $z \sim 2.3$ from van Dokkum et al. (2008, hereafter vD+08, purple solid line); (2) compact Lyα break

[17] Here, we switch to SFR instead of using sSFR, to directly compare our results with the literature.

[18] $\log({\rm SFR}/M_\odot\ {\rm yr}^{-1}) = \log({\rm sSFR\ Gyr}^{-1}) + \log(M_*/M_\odot) - 9$.

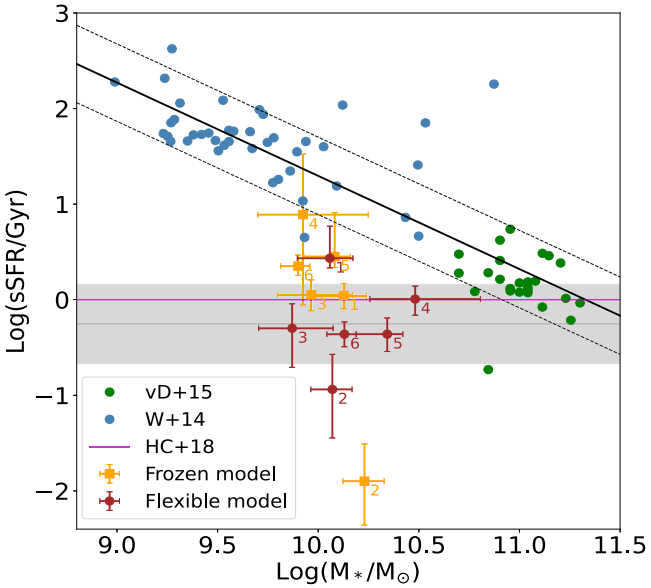

Figure 5. The sSFR–M_* relation for the six pBNs from both the flexible model (red dots with error bars) and the frozen model (orange squares with error bars). The gray horizontal line represents the mean log(sSFR), with the shaded area indicating the 1σ confidence interval. The numbers 1–6 represent the six nuggets in the order listed in Table 1. For comparative purposes, we have also plotted the compact massive SFGs (green dots) within the redshift range of $2.0 < z < 2.5$ (van Dokkum et al. 2015, vD+15), the compact LBGs (blue dots) at $z \sim 3$ (Williams et al. 2014, W+14) and the up limit of the log(sSFR) for pBNs (magenta line) in CANDELS at redshift $1.4 < z < 2.0$ (Huertas-Company et al. 2018, HC+18). All mass estimates have been rescaled to be compatible with a Chabrier IMF. The compact massive SFGs and the LBGs are distributed along a single relation (solid black line), with the 1σ confidence interval ∼0.4 (dashed black lines). whereas the pBNs are situated systematically below this line, suggesting a transition out of the star-forming phase.

galaxies (LBGs) at $z \sim 3$ from W+14 (blue crosses); (3) normal active galaxies (green dashed lines) and passive galaxies (red dashed lines) at z = 1.75 from van der Wel et al. (2014, hereafter vdW+14) similar data can also be found in Mowla et al. 2019 and Nadolny et al. 2021). All stellar masses are corrected to a Chabrier IMF, consistently with our choice. From Figure 4, we see that our lensed pBNs are located away from the size–mass relationship of the SFGs (green dashed line). Rather, they mainly occupy the location of the compaction peak of blue nuggets at $z < 2.5$ (blue boxes) and $z > 3$ (green boxes) predicted by simulations (Z+15). This shows that the typical masses and sizes of the six systems are fully compatible with post-compacted galaxies. The log-linear mass–size relation for the pBNs and red nuggets, $\log(R_{\rm eff}) = \alpha \log(M_*)$, gives a slope $\alpha \sim 0.66$. Compared to "red nuggets" and passive galaxies at similar redshift ($z = 1.5$ and $z = 1.75$ respectively), the lensed pBNs are generally aligned to the size–mass relations of both samples, while they all seem offset by ∼0.5 dex with respect to the red nugget samples at $2 < z < 3$ (vD+08), possibly due to the earlier formation of these higher-z systems. Finally, the pBN sample looks aligned to the compact LBGs (blue crosses), which are believed to be blue nuggets with strong star formation, $\log(\mathrm{sSFR\ Gyr^{-1}}) > 0.5$ or $\log(\mathrm{SFR}/M_\odot\ \mathrm{yr^{-1}}) > 3$ (W+14); however, the slope of these latter is 0.38 (light blue line in Figure 4), slightly flatter than that of the pBNs plus red nuggets. This confirms the scenario that pBNs share properties of both active and passive compact galaxies because the quenching occurs after compaction in the pBN phase and the six pBN systems seem indeed in the transition from typical blue nugget systems to red nuggets. The turning knee of the two size–mass relationships appears at the location of $\log(M_*/M_\odot) \sim 10$–10.5. This has been indicated as a characteristic mass scale for a structural transition of the red-blue nugget systems (see, e.g., Lapiner et al. 2023), mainly because of the dominance of the wet processes (gas inflows) at lower mass scales, and the dry processes (e.g., dry mergers) acting at larger mass scales. Finally, in the same Figure 4, we show, as lighter blue data, the results of the frozen model for comparison. We see that two of the systems deviate from the size–mass relation. If we take their sSFRs at face value (see Figure 5), these two systems turn out to be very close or superior to the upper sSFRs (or SFR) limits of quiescent systems or pBNs discussed in the literature (e.g., Johnston et al. 2015; HC+18, see above). This leaves us with the possibility that two of the six systems are still in the transition to the blue nugget phase, as also suggested by their Σ_1 (see below).

On the right panel of Figure 4, we show the density inside 1 kpc versus stellar mass of the pBNs. Here, the alignment with red nuggets is even more evident than the size–mass relation on the left panel. The log-linear relation gives a slope of 0.65, fully consistent with the one found for the quiescent galaxies in the redshift range $1.4 < z < 2$ by B+17, also reported in Figure 4—right. This latter work also shows that the compact SFGs follow the sequence of the quiescent galaxies, consistent with the scenario that compaction produces a fast core growth, causing normal SFGs to move up from the main SFG sequence (see blue line reported in Figure 4—right). In this respect, the two frozen model outliers seen above occupy the region of the transition from the star-forming systems to compact SFGs, suggesting that they might even still be going through compaction. This indicates that the classification of these two systems as pBNs is the most insecure one, and they might therefore need a spectroscopic follow-up.

Figure 5 presents the log(sSFR) as a function of the stellar mass $\log(M_*)$ for the six pBNs, using both the flexible model (red dots with error bars) and the frozen model (orange dots). The mean log(sSFR), calculated to be −0.253 Gyr, is shown by the gray horizontal line. The 1σ confidence interval, determined by the standard error ($\sigma = 0.42$), is reported as a shaded region. This standard error coincides with typical uncertainties (∼0.4 dex) in sSFR estimates derived from nine-band KiDS photometry and photo-zs (see Xie et al. 2023), hence showing that the dominating effect on the scatter comes from the SED procedure rather than the lensing/photometry errors. In the same figure, we also plot compact massive SFGs(green dots) within the redshift range $2.0 < z < 2.5$ from vD+15, and the compact LBGs (blue dots) at $z \sim 3$, from W+14 for comparison, similarly to what showed in Figure 4. Both these SFG samples clearly sit on a common log–log linear trend, represented by black solid line, with a standard deviation of $\sigma = 0.41$, represented by black dashed lines. On the other hand, all pBNs are observed to lie below the fitted line to the star-forming sample, suggesting that the star-forming activities of pBNs are indeed weaker than those of typical SFGs. The magenta horizontal line indicates the upper limit of the typical log(sSFR) found for pBNs in CANDELS (HC+18) at redshift $1.4 < z < 2.0$. Most of our pBNs are consistent this line. Overall we tend to conclude that the final results are independent on the lensing priors (frozen versus flexible) adopted.

5. Conclusions

We have collected six strong gravitational lens systems with blue pointlike lensed images from the catalog of "high-quality candidates" from the KIDS Survey (Petrillo et al. 2019; Li et al. 2020, 2021). We have performed ray-tracing modeling in the nine-band imaging data and derived the intrinsic multiband photometry of the sources. Via photo-z and stellar population analysis, we have confirmed that (1) the systems are genuine SL events; and (2) the background sources of these six SL systems are very likely pBNs because of their very small effective radii, large mass, and low sSFRs, although, (3) depending on the priors on the ray-tracing model (i.e., whether one leave almost multiband parameters free or fixed to the highest quality r-band model), there is a possibility that two of the six systems are still in a transition phase. In particular, from the perspective of the SFR–M_* and sSFR–Σ_1 relations, the six pBNs are well consistent with observations of compact low sSFR objects in Johnston et al. (2015) and HC+18. In terms of the $R_{\rm eff}$–M_*, Σ_1–M_*, and sSFR–M_* relations, these pBNs do not follow the main sequence of SFGs but align well with the relation of the passive, compact red nuggets at similar redshifts. Also, they sit on the tail of the size–mass relation of the compact LBGs from W+14. However, the two systems showing up as outliers in the frozen priors' model, taken at face value, possess a SFR which is compatible with ongoing star formation and occupy the region of these scaling relations of transient objects from normal SFGs to the pBN systems. Overall, considering the continuity of the size–mass relations of the compact SFGs and the red nuggets, the "confirmed" pBNs (especially looking at the flexible prior results) sit in a knee located at $\log(M_*/M_\odot) \sim 10.5$ consistently with the presence of a characteristic mass for wet compaction (Lapiner et al. 2023).

All these facts together indicate that the pBNs are in a transition phase between the blue and red nuggets, as all structural scaling relations are set to become red nuggets, but with some residual ongoing star formation. This latter is seen, for the two systems in Napolitano et al. (2020), from weak emission lines coexisting however with stellar absorption lines typical of old stellar populations. Finally, taking the modeled Sérsic indexes of these six pBNs at face value, regardless of the adopted prior, they are generally smaller ($n < 3$) than the predictions from simulations ($n > 3$) or observations of red nuggets (D+09). Nevertheless, these values are compatible with the scenario that, during the pBN phase, i.e., after the gas is depleted from the center, leaving behind a compact passive nugget, a new extended rotation-supported gas disk/ring can develop (Toft et al. 2017; Lapiner et al. 2023). The only way to obtain a more detailed model and shed light on this aspect would be to obtain higher-quality images.

This work is based on a small number of objects (possibly all we can expect, according to N+20) found in the KiDS footprint, but other candidates have been identified in the footprint of other surveys like Hyper Suprime-Cam (Jaelani et al. 2020) and Dark Energy Survey (Jacobs et al. 2019). We plan to extend this analysis to other systems soon, and possibly add spectroscopic data in order to further observationally support the understanding of the pBN phase, which is crucial in the morphological transformation of galaxies in their early phase of evolution.

Acknowledgments

R.L. and R.L. acknowledge the support of the National Nature Science Foundation of China (Nos. 12203050, 11988101,11773032,12022306), the science research grants from the China Manned Space Project (CMS-CSST-2021-A01) and the support from K.C.Wong Education Foundation. N.R.N. acknowledges financial support from the Research Fund for International Scholars of the National Science Foundation of China, grant No. 12150710511 (BluENeSS). C.T. acknowledges the INAF grant 2022 LEMON. Xiaotong Guo is supported by National Nature Science Foundation of China (No.12303017) and Anhui Provincial Natural Science Foundation project (No.2308085QA33).

Appendix
Multiband Ray-tracing Frozen Model Results

In this appendix, we report the results of the frozen prior model described in Section 3.1, and compare them with the flexible prior results. In Table A1, we report the full multiband parameters for the flexible model in Table 1. We can measure the mean and the standard deviation of the source magnitudes derived from the two models as a measure of the average consistency from the two sets of magnitudes, and find these to be -0.002 ± 0.2139. This shows no systematics between the two models and a statistical error consistent with typical photometric errors for ground-based observations. The corresponding photo-zs are also compared with the ones from the flexible model in the left panel in Figure A1: these also show a rather large scatter but within the typical uncertainties expected for ground-based photo-zs (e.g., van den Busch et al. 2020; Amaro et al. 2021; Li et al. 2022). In the right panel of Figure A1, we compare the physical effective radii of the galaxies, measured in kiloparsec, along with their respective error bars. Our analysis reveals that the effective radii derived from the two different models are in close agreement, with a

Table A1
Source Properties from the Multiband Ray-tracing Frozen Model

ID	$R_{\rm eff}$ (arcsec)	b/a	p.a. (deg)	n	u (mag)	g (mag)	r (mag)	i (mag)	Z (mag)	Y (mag)	J (mag)	H (mag)	K_s (mag)
J023929−321129	0.051 ± 0.002	0.48 ± 0.03	90	2.6 ± 0.1	23.84	23.46	23.30	23.34	23.29	23.46	23.17	22.73	⋯
J122456+005048[a]	0.042 ± 0.002	0.41 ± 0.02	98	2.0 ± 0.1	⋯	23.97	23.52	22.87	22.34	22.13	21.79	21.60	21.47
J224546−295559	0.056 ± 0.005	0.45 ± 0.06	16	3.4 ± 0.3	24.10	23.81	23.71	23.75	23.70	23.15	22.57	⋯	⋯
J230226−335637	0.138 ± 0.007	0.56 ± 0.04	68	2.4 ± 0.3	23.48	23.06	23.08	22.99	22.78	22.73	22.20	22.17	⋯
J232940−340922[a]	0.077 ± 0.012	0.29 ± 0.03	168	1.8 ± 0.8	⋯	23.64	23.44	23.36	23.33	22.69	22.36	22.15	21.87
J234804−302855	0.167 ± 0.008	0.38 ± 0.03	71	1.3 ± 0.2	23.95	23.64	23.68	23.62	23.94	23.37	22.82	22.70	⋯

Note. Column content is as in Table 1.

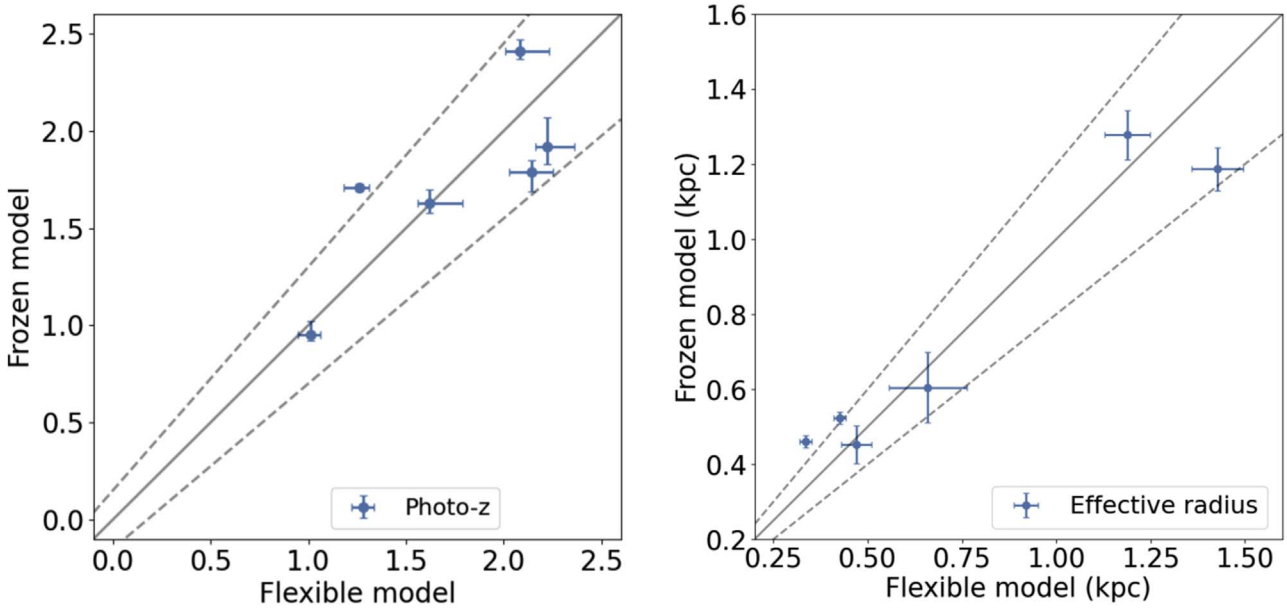

Figure A1. Comparison of relevant parameters obtained from the frozen model and flexible model. Left: photo-zs. The black solid line represents the 1:1 relation of the two photo-zs, while the two black dashed lines show the 15% bias defined as $|\delta z| = |z_{\rm froz} - z_{\rm flex}|/(1 + z_{\rm flex})$. Right: effective radius. The solid line is again the 1-to-1 relation, while the dashed lines represent the 20% bias defined as $|\delta r| = |r_{\rm froz} - r_{\rm flex}|/r_{\rm flex}$.

discrepancy of $\lesssim$20%. It is important to highlight that this deviation primarily comes from the lensing model itself, rather than the uncertainties associated with the photo-zs. To further illustrate this point, we examined the case of J224546-295559, which displays the most significant photo-z discrepancy between the flexible model and the frozen model, $\Delta z = 0.45$. Even in this extreme case, we have estimated that the impact of this photo-z discrepancy on the effective radius is minimal, contributing to only a 1.6% uncertainty. Finally, we cumulatively compare the stellar masses and the sSFRs, which have been shown in Section 5 but have not been discussed in depth. As expected, the magnitude and photo-z errors propagate more dramatically on the stellar population parameters, especially sSFRs, with a typical deviation of the order of $\sim$0.2 dex for stellar masses and $\sim$0.41 dex for sSFRs. These are not dissimilar to typical statistical errors found for stellar population parameters using normal KiDS galaxies (e.g., $\sim$0.4 dex, Xie et al. 2023), although they are big enough to move galaxies above the upper limit assumed to separate compact star-forming systems from compact quenched systems in observations (i.e., $\log(\mathrm{sSFR\ Gyr^{-1}}) \sim 0$, see again Johnston et al. 2015 and HC+18). However, all systems remain compatible with a "quenching" scenario, as they are situated below the mean sequence of compact SFGs (see Figure 5). To be conservative, and considering the typical uncertainties on sSFRs (marked as the gray shaded region) and the results of the frozen priors at face value, two of the six systems have both sizes and sSFRs that deviate from the expectation to be pBN (see a more detailed discussion in Section 4).

ORCID iDs

Rui Li https://orcid.org/0000-0002-3490-4089
Nicola R. Napolitano https://orcid.org/0000-0003-0911-8884
Linghua, Xie https://orcid.org/0000-0002-2831-8630
Xiaotong Guo https://orcid.org/0000-0002-2338-7709
Alexey Sergeyev https://orcid.org/0000-0003-3425-5178
Crescenzo Tortora https://orcid.org/0000-0001-7958-6531
Chiara Spiniello https://orcid.org/0000-0002-3909-6359
Léon V. E. Koopmans https://orcid.org/0000-0003-1840-0312

References

Amaro, V., Cavuoti, S., Brescia, M., et al. 2021, in Intelligent Astrophysics, ed. I. Zelinka, M. Brescia, & D. Baron, Vol. 39 (Berlin: Springer), 245
Barro, G., Faber, S. M., Koo, D. C., et al. 2017, ApJ, 840, 47
Barro, G., Faber, S. M., Pérez-González, P. G., et al. 2013, ApJ, 765, 104
Barro, G., Faber, S. M., Pérez-González, P. G., et al. 2014, ApJ, 791, 52
Boquien, M., Burgarella, D., Roehlly, Y., et al. 2019, A&A, 622, A103
Bruzual, G., & Charlot, S. 2003, MNRAS, 344, 1000
Cattaneo, A., Faber, S. M., Binney, J., et al. 2009, Natur, 460, 213
Chabrier, G. 2003, PASP, 115, 763
Costantin, L., Pérez-González, P. G., Méndez-Abreu, J., et al. 2021, ApJ, 913, 125
Damjanov, I., McCarthy, P. J., Abraham, R. G., et al. 2009, ApJ, 695, 101
de Jong, J. T. A., Verdoes Kleijn, G. A., Kuijken, K. H., & Valentijn, E. A. 2013, ExA, 35, 25
de Vaucouleurs, G. 1948, AnAp, 11, 247
Dekel, A., & Burkert, A. 2014, MNRAS, 438, 1870
Dekel, A., Sari, R., & Ceverino, D. 2009, ApJ, 703, 785
Dekel, A., & Silk, J. 1986, ApJ, 303, 39
Edge, A., Sutherland, W., Kuijken, K., et al. 2013, Msngr, 154, 32
Gu, A., Huang, X., Sheu, W., et al. 2022, ApJ, 935, 49
Huertas-Company, M., Primack, J. R., Dekel, A., et al. 2018, ApJ, 858, 114
Ilbert, O., Arnouts, S., McCracken, H. J., et al. 2006, A&A, 457, 841
Jacobs, C., Collett, T., Glazebrook, K., et al. 2019, ApJS, 243, 17
Jaelani, A. T., More, A., Sonnenfeld, A., et al. 2020, MNRAS, 494, 3156
Johnston, R., Vaccari, M., Jarvis, M., et al. 2015, MNRAS, 453, 2540
Kormann, R., Schneider, P., & Bartelmann, M. 1994, A&A, 284, 285
Kuijken, K., Heymans, C., Dvornik, A., et al. 2019, A&A, 625, A2
Langeroodi, D., Sonnenfeld, A., Hoekstra, H., & Agnello, A. 2023, A&A, 669, A154
Lapi, A., Pantoni, L., Zanisi, L., et al. 2018, ApJ, 857, 22
Lapiner, S., Dekel, A., Freundlich, J., et al. 2023, MNRAS, 522, 4515
Li, R., Napolitano, N. R., Feng, H., et al. 2022, A&A, 666, A85
Li, R., Napolitano, N. R., Tortora, C., et al. 2020, ApJ, 899, 30
Li, R., Napolitano, N. R., Spiniello, C., et al. 2021, ApJ, 923, 16
Liu, F. S., Jiang, D., Guo, Y., et al. 2016, ApJL, 822, L25
Marques-Chaves, R., Schaerer, D., Álvarez-Márquez, J., et al. 2022, MNRAS, 517, 2972

Mowla, L. A., van Dokkum, P., Brammer, G. B., et al. 2019, ApJ, 880, 57
Murray, N., Quataert, E., & Thompson, T. A. 2005, ApJ, 618, 569
Nadolny, J., Bongiovanni, Á., Cepa, J., et al. 2021, A&A, 647, A89
Napolitano, N. R., Li, R., Spiniello, C., et al. 2020, ApJL, 904, L31
Newman, A. B., Ellis, R. S., Bundy, K., & Treu, T. 2012, ApJ, 746, 162
Nipoti, C., Treu, T., Leauthaud, A., et al. 2012, MNRAS, 422, 1714
Oldham, L., Auger, M. W., Fassnacht, C. D., et al. 2017, MNRAS, 465, 3185
Oser, L., Naab, T., Ostriker, J. P., & Johansson, P. H. 2012, ApJ, 744, 63
Petrillo, C. E., Tortora, C., Vernardos, G., et al. 2019, MNRAS, 484, 3879
Posti, L., Nipoti, C., Stiavelli, M., & Ciotti, L. 2014, MNRAS, 440, 610
Renzini, A. 2006, ARA&A, 44, 141
Sergeyev, A., Spiniello, C., Khramtsov, V., et al. 2018, RNAAS, 2, 189
Sersic, J. L. 1968, Atlas de Galaxias Australes (Cordoba: Observatorio Astronomico)
Spiniello, C., Tortora, C., D'Ago, G., et al. 2021, A&A, 646, A28
Sutherland, W., Emerson, J., Dalton, G., et al. 2015, A&A, 575, A25
Tacchella, S., Dekel, A., Carollo, C. M., et al. 2016, MNRAS, 458, 242
Tessore, N., Bellagamba, F., & Metcalf, R. B. 2016, MNRAS, 463, 3115
Toft, S., Zabl, J., Richard, J., et al. 2017, Natur, 546, 510
Trager, S. C., & Somerville, R. S. 2009, MNRAS, 395, 608
van den Busch, J. L., Hildebrandt, H., Wright, A. H., et al. 2020, A&A, 642, A200
van der Wel, A., Franx, M., van Dokkum, P. G., et al. 2014, ApJ, 788, 28
van Dokkum, P. G., Franx, M., Kriek, M., et al. 2008, ApJL, 677, L5
van Dokkum, P. G., Nelson, E. J., Franx, M., et al. 2015, ApJ, 813, 23
Whitaker, K. E., Kriek, M., van Dokkum, P. G., et al. 2012, ApJ, 745, 179
Williams, C. C., Giavalisco, M., Cassata, P., et al. 2014, ApJ, 780, 1
Worthey, G. 1994, ApJS, 95, 107
Xie, L., Napolitano, N. R., Guo, X., et al. 2023, SCPMA, 66, 129513
Zolotov, A., Dekel, A., Mandelker, N., et al. 2015, MNRAS, 450, 2327